Post hoc analysis of passive cavitation imaging for classification of histotripsy-induced liquefaction *in vitro*

Kenneth B. Bader, Kevin J. Haworth, *Member, IEEE*, Adam D. Maxwell, *Member, IEEE*, and Christy K. Holland *Member, IEEE*

Abstract—**Histotripsy utilizes focused ultrasound to generate bubble clouds for transcutaneous tissue liquefaction. Image guidance of histotripsy pulses is required to provide spatially resolved monitoring of treatment progress. The aim of this study was to investigate the feasibility of plane wave B-mode and passive cavitation images to be used as binary classifiers of histotripsy-induced liquefaction. Prostate tissue phantoms were exposed to histotripsy pulses over a range of pulse durations (5 – 20 μs) and peak negative pressures (12 – 23 MPa). Acoustic emissions were recorded during the insonation and beamformed to form passive cavitation images. Plane wave B-mode images were acquired following the insonation to detect the hyperechoic bubble cloud. Phantom samples were sectioned and stained to delineate the liquefaction zone. Correlation between passive cavitation and plane wave B-mode images and the liquefaction zone was assessed using receiver operating characteristic (ROC) curve analysis. Liquefaction of the phantom was observed for all insonation conditions. The area under the ROC (0.94 vs. 0.82), accuracy (0.90 vs. 0.83), and sensitivity (0.81 vs. 0.49) was greater for passive cavitation images relative to B-mode images ($p < 0.05$) along the azimuth of the liquefaction zone. The specificity was greater than 0.9 for both imaging modalities. These results here demonstrate a stronger correlation between histotripsy-induced liquefaction and passive cavitation imaging compared to plane wave B-mode imaging, albeit with limited passive cavitation image range resolution.**

Index Terms— **Cavitation, Passive Cavitation Imaging, Histotripsy, Classification**

I. INTRODUCTION

High-intensity focused ultrasound (HIFU) is utilized clinically for noninvasive ablation of uterine fibroids, bone metastases, and prostate tissue [1]. Clinical HIFU devices induce cell death by hyperthermia and rely on magnetic resonance (MR) thermometry or diagnostic ultrasound to monitor treatment progress [2]. Histotripsy is an alternative focused ultrasound therapy that incites bubble clouds to liquefy (i.e. homogenize) tissue at depth mechanically rather than thermally [3], [4]. Preclinical studies have investigated histotripsy for treatment of deep vein thrombosis [5]-[7], fetal septal defects [8], kidney stones [9], liver cancer [10], and benign prostatic hyperplasia [11]. A clinical trial is currently underway whose primary outcome is to assess the safety of histotripsy technology to treat benign prostatic hyperplasia [12].

[1]Histotripsy image guidance is performed by visualizing bubbles clouds or assessing changes in tissue structure. Bubble clouds appear hyperechoic on B-mode imaging [13], and can be detected with T2-weighted MR images [14], [15]. These imaging modalities indicate the presence of cavitation, but do not indicate if the mechanical oscillation of the bubbles within the cloud are sufficient to induce tissue liquefaction. The bubble cloud can also undergo significant temporal evolution over the course of a traditional B-mode image acquisition [16]-[18]. Plane wave B-mode imaging captures the bubble cloud position and area at a single instance in time [19]-[21], thereby eliminating artifacts associated with temporal averaging. Nonetheless, the echogenicity of the bubble clouds has high inter-sample variability, limiting the utility for monitoring histotripsy [13], [22]. Changes in tissue structure initiated by the bubble cloud have been assessed with B-mode imaging [13], ultrasound elastography [23], bubble-induced color Doppler [22], [24], and T2-weighted MR imaging [14], [25]. The observed changes occur after tissue liquefaction, preventing assessment of treatment efficacy during the active histotripsy treatment.

Passive cavitation imaging (PCI) maps the power of acoustic emissions generated by the mechanical oscillations of bubbles [26], [27]. Passive ultrasound imaging techniques have previously been employed to monitor thermal ablation with focused ultrasound [28]-[30], ultrasound-mediated drug delivery [31]-[34], histotripsy bubble clouds [19], and clot liquefaction with histotripsy [7]. In this study, post hoc analysis of passive cavitation imaging (PCI) was investigated to classify the location of histotripsy-induced liquefaction throughout a tissue-mimicking phantom. The images were also analyzed to determine the relative utility of PCI for characterizing bubble cloud dynamics.

II. METHODS AND MATERIALS

A. Prostate Phantom Production

The dimension of histotripsy liquefaction zones generated in tissue phantoms and *ex vivo* tissue are similar [35]. Thus, tissue phantoms have been utilized extensively in pre-clinical

histotripsy studies [15], [36]-[38]. The current clinical target for histotripsy is benign prostatic hyperplasia [12]. Therefore, a prostate-mimicking tissue phantom was used for these studies following a previously developed protocol [39]. Briefly, the phantom was composed of agar (3.7 g), deionized water (147.2 mL), n-propanol (12.8 mL), and evaporated milk (240 mL). Commercially available evaporated milk (Meijer Brand, Meijer, Inc., Grand Rapids, MI, USA) was filtered (pore size 100 µm, part number 10340810, Whatman, Maidstone, United Kingdom), and gently stirred on a hot plate to reach a final temperature of 55°C. Agar powder (A9539 Sigma-Aldrich Co. St. Louis, MO, USA) was dissolved into a 0.2 µm filtered, deionized water (NANOPure, Barnstead International, Dubuque, IA, USA) and n-propanol solution by heating in 30 s increments in a microwave (1 kW power) until clear. The heated agar/n-propanol solution was placed in a heated (50°C) ultrasonic cleaning bath for 30 min while continuously evacuating at 2 kPa. The degassed agar/n-propanol solution was combined with the heated evaporated milk, poured into a mold, and allowed to solidify at 5°C. This formation has previously been shown to replicate the density, sound speed, and frequency-dependent acoustic attenuation spectra of *ex vivo* prostate tissue [39]. The dynamics of histotripsy bubble clouds can be significantly altered by the medium stiffness [37], [40]. The concentration of agar was adjusted so that the elastic modulus of the phantom was 44 ± 0.4 kPa [41], similar to that observed in benign prostatic hyperplasia [42]-[44]. The mold contained hyperechoic fiducial markers (0.5-mm outer diameter nylon filament, Berkley, Spirit Lake, IA, USA) to enable registration of ultrasound and phantom images. Five phantoms were made for each set of insonation conditions.

B. Histotripsy Insonation

Histotripsy pulses were generated with a 1-MHz, 8-element annular array with a 10-cm aperture and 9-cm focal length (Imasonic, Voray sur l'Ognon, France). All elements of the transducer were simultaneously driven in parallel by a custom designed and built class D amplifier and matching network [45]. The transducer was calibrated in water at the focus for peak negative pressures up to 18.3 MPa with a fiber optic hydrophone (FOPH 2000, RP Acoustics, e.K., Leutenbach, Germany) [7]. Direct calibration of the histotripsy transducer was not possible for greater peak negative pressures due to cavitation, and the peak negative pressure was estimated following Maxwell *et al.* [46]. A total of 2000 histotripsy pulses of 5, 10, or 20 µs duration were delivered to each phantom at a pulse repetition frequency of 20 Hz (10, 20, or 40 ms total histotripsy exposure time, respectively). The focal peak negative pressure of the pulse was 12, 15, 18, 20, or 23 MPa, derated based on the acoustic attenuation coefficient of the phantom assuming a 1 MHz fundamental frequency (0.46 dB/cm) [39]. The derated peak positive pressures were estimated following Canney *et al.* [47] to be 77, 93, 105, 116, and 123 MPa. The two largest pressure levels, beyond the calibration of the transducer calibration, were estimated based on numerical simulation [48]. The insonation conditions

employed in this study span those previously employed for histotripsy [3], [4].

C. Passive Cavitation and Plane Wave B-mode Imaging

Passive cavitation images were used to map the power of acoustic emissions generated by histotripsy-induced cavitation. Cavitation emissions were passively recorded during the histotripsy insonation with an L7-4 imaging array (ATL, Bothell, WA, USA) using an ultrasound research scanner (Vantage 256, Verasonics, Inc., Kirkland, WA, USA). The imaging array was placed 30 mm from the focus of the histotripsy transducer, and oriented to monitor cavitation activity along the central axis of the histotripsy transducer (azimuthal axis of the imaging array, Fig. 1A). Pixel values were assigned to location $\vec{r}$ using frequency selective beamforming based on the receive acoustic power, P, following Haworth *et al.* [49]:

$$P(\vec{r}) = \frac{1}{T_H} \sum_{\omega=\omega_0}^{\omega_f} \left| \sum_{n=1}^{N} S_n(\omega) \exp\left(i\omega \frac{\vec{r}_n - \vec{r}}{c} \right) \right|^2 \qquad (1)$$

where S_n is the frequency domain representation of the signal at angular frequency ω on the nth element of the passive array at location $\vec{r}_n$, N is the total number of elements, and T_H is the duration of the histotripsy pulse in microseconds. The units of P in (1) are $mV^2/\mu s$. Acoustic emissions generated by histotripsy-induced bubble clouds have a broad frequency spectrum [7]. Thus, the passive cavitation images were formed using the acoustic emissions within the bandwidth of the imaging array (2.5 to 8.5 MHz, corresponding to ω_0 and ω_f in (1), respectively).
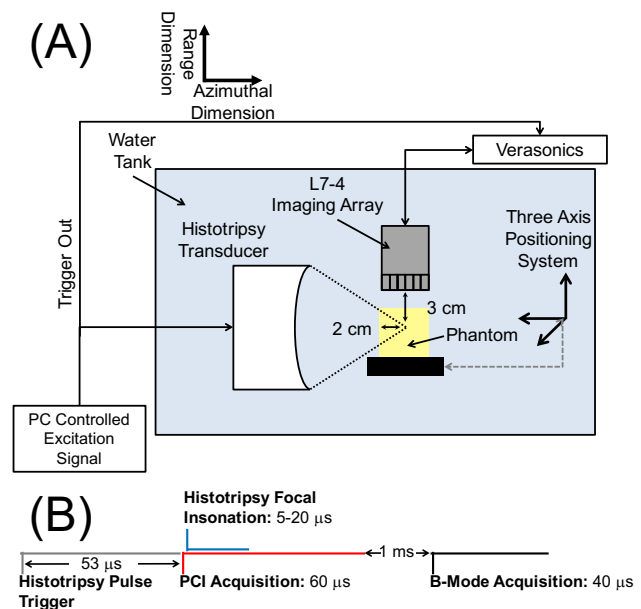
Fig. 1 (A) Side view of experimental set up for histotripsy liquefaction of the prostate tissue phantom. An L7-4 imaging array was oriented to monitor cavitation activity along the azimuthal/range plane of the histotripsy transducer (9-cm focal length, 10 cm outer diameter). (B) Timing diagram for the acquisition of passive cavitation emissions and plane wave B-mode images during histotripsy insonation of the prostate tissue phantom. Passive acquisition was initiated 5 µs before the histotripsy pulse reached the focus.

Figure 2: (Top panel) Passive Cavitation Image (PCI) registered with processed phantom image. The liquefaction zone border is outl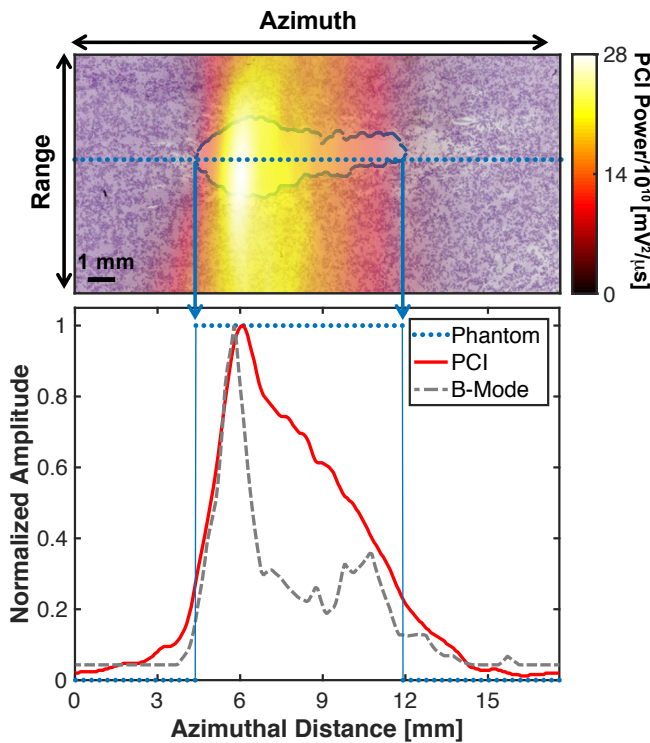ined in blue. The phantom image was analyzed along the entire azimuth through the liquefaction zone in 0.3 mm increments (dotted line). (Bottom panel) Comparison of the PCI and plane wave B-mode image along the dotted line in the top panel and binary phantom image. For the phantom, values of 1 indicate liquefaction, and values of 0 indicate intact phantom. The histotripsy pulse (1 MHz center frequency, 10 μs pulse duration, 18 MPa peak negative pressure) was propagating from left to right in the image.

The same imaging array was employed to acquire plane wave B-mode images following passive acquisition of cavitation emission (Fig. 1B) [50]. The plane wave B-mode images were acquired using similar parameters as prior studies in order to provide a comparison to PCI [18]-[21].

The imaging sequence was triggered by the histotripsy transmit (Fig. 1B). Passive detection of cavitation emissions, used for PCI, was acquired over a 60 μs duration starting 5 μs prior to the histotripsy insonation reaching the focus. The plane wave B-mode imaging pulse was initiated approximately 1 ms after the histotripsy focal insonation, a delay consistent with a previous study employing plane wave B-mode imaging to monitor histotripsy bubble clouds [20]. Interference patterns between the imaging and therapy pulses prevent meaningful analysis of bubble clouds in plane wave B-mode images acquired during the histotripsy insonation. Due to data transfer rate limitations, passive cavitation and plane wave images were acquired once every fifth histotripsy pulse (4 Hz). The acoustic power was summed pixel by pixel across all passive cavitation images acquired for a given data set to create a cumulative passive cavitation image. Likewise, the grayscale values were summed pixel by pixel across all acquired plane wave B-mode images for a given data set to create a cumulative plane wave B-mode image. A separate set of experiments were also performed using ultrafast plane wave B-mode imaging (11.5 kHz) to assess the change in the bubble

cloud grayscale value after completion of the histotripsy excitation.

D. Experimental protocol

Phantoms were degassed for two hours in deionized water at a partial pressure of 2 kPa, after which they were affixed to a three-axis positioning system (TDC001, Thorlabs Inc, Newton, NJ, USA) immersed in a tank of degassed (20% dissolved oxygen), filtered (10 μm pore size) water. Bubble clouds generated by 5 μs histotripsy pulses in the water tank were visualized with plane wave B-mode images. The cloud location in the image was denoted as the free field focus of the histotripsy transducer [5], [10]. The phantom was then positioned such that the histotripsy transducer focus was at a depth of 2 cm into the phantom (Fig. 1A). For each phantom, three regions were insonated with 2000 histotripsy pulses. Each insonation region was separated by 8 mm, and the exposure conditions were randomized. The distance between the histotripsy focus and the imaging array was fixed at 3 cm (Fig. 1A). Four-hundred frames of passive cavitation and plane wave B-mode images were acquired per data set. Emissions were processed offline to generate passive cavitation images. In total, 75 liquefaction zones were generated in 25 different phantoms.

E. Phantom Processing

After insonation, each liquefied zone in the phantom was sectioned and dehydrated with a series of 12-hour graded ethanol steps (v/v: 70, 80, 95, and 100%). The dehydrated phantom section embedded in paraffin, sectioned (5-μm thickness), and processed with a periodic acid-Schiff (PAS) stain (Poly Scientific R&D Corporation, Bay Shore, NY, USA). Digital bright field images of the stained phantoms were obtained using a digital slide scanner (Aperio AT2, Leica Biosystems; St. Louis, MO) at 20 times magnification. A custom edge detection routine using a Canney filter was implemented in MATLAB (The Mathworks, Natick, MA) to delineate the liquefaction zone borders.

F. Comparison of Passive Cavitation and Plane Wave B-Mode Images with Processed Phantom Images

Cumulative passive cavitation and plane wave B-mode images were registered with the PAS-stained phantom images using a custom geometric transformation in MATLAB based on the hyperechoic nylon filaments. Receiver operator characteristic (ROC) analysis was performed to compare passive cavitation and plane wave B-mode images to stained phantom optical images. The analysis was performed for all pixels in the image at a fixed range depth of 30 mm (i.e. Fig. 2 from 0 to 17.6 mm, 0.3 mm pixel spacing indicated by the dotted line). Only pixels corresponding to a range depth of 30 mm were analyzed because of the limited range resolution inherent to the beamforming algorithm employed in (1) [33]. A pixel was assigned a true positive (false positive) value when it corresponded to a location with liquefied phantom and the acoustic power or grayscale value was greater than (less than) a pre-defined threshold value. A pixel was assigned a true negative (false negative) value when it corresponded to intact phantom and the acoustic power or grayscale value was less

Azimuth

Range

Stained Phantom

(A)

B-mode Imaging Overlay

(B)

Grayscale Value/10^8

PCI Overlay

(C)

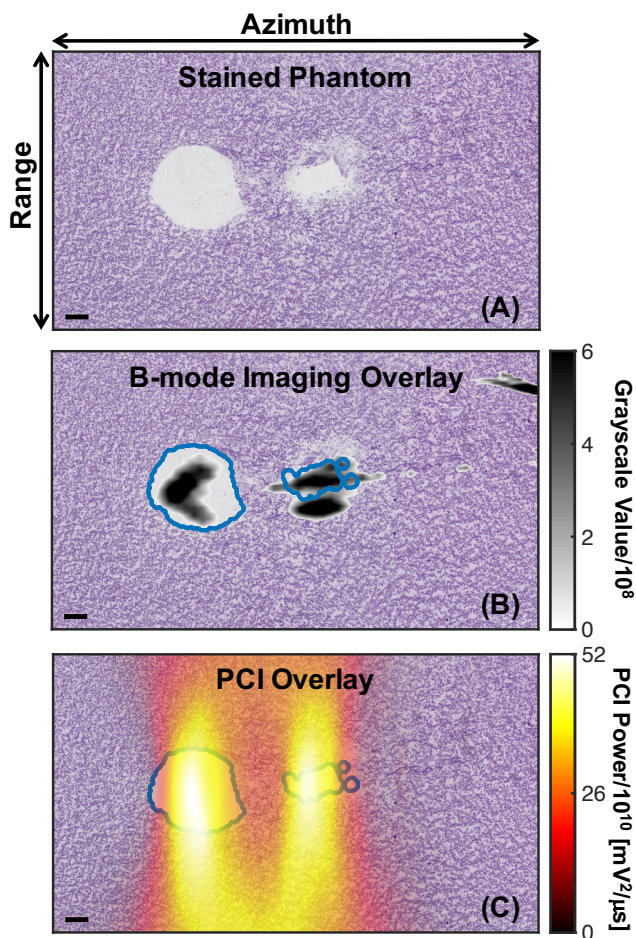PCI Power/10^{10} [mV²/μs]

Fig 3: (A) Phantom after PAS stain to demark liquefaction (white) generated by histotripsy insonation. (B) Comparison of co-registered plane wave B-mode image and processed phantom image. (C) Comparison of co-registered Passive Cavitation Image (PCI) and processed phantom image. Both the PCI and plane wave B-mode images were summed over 400 frames (the duration of the histotripsy insonation) to create cumulative images. For panels B and C, the liquefaction zone boarders are outlined in blue. The histotripsy pulse (1-MHz center frequency, 5-μs pulse duration, 23-MPa peak negative pressure) propagated from left to right in the image. The bar in the lower left corner of each image corresponds to 1 mm. The azimuthal/range dimensions of the imaging plane are indicated in the top panel.

than (greater than) a pre-defined threshold value [28], [29]. Cavitation emissions are often reported on a decibel scale [51]-[54]. Thus, ROC curves were computed for both non-compressed and logarithmically compressed acoustic powers and grayscale values.

G. Statistical Analysis

Statistical analysis was performed using the MATLAB Statistical Toolbox. The null hypothesis that the area under the receiver operator characteristic (AUROC) was equal to 0.5, indicating the technique did no better than random guessing, was tested following Hanley and McNeil [55]. The threshold acoustic power or grayscale value for phantom liquefaction was extracted from the ROC following Zweig and Campbell [56]. The accuracy, sensitivity, specificity, positive predictive value, and negative predicative value were extracted from the ROC curve at the threshold point. Confidence bands of the ROC were extracted with the use of a bootstrap to estimate the standard deviation of these metrics [57]. Significant

differences in the AUROC were determined following DeLong *et al.* [58]. The number of independent measurements, based on the –6 dB width of the L7-4 imaging array, was estimated following Haworth *et al.* [29]. Differences between passive cavitation and plane wave B-mode imaging values of the accuracy, sensitivity, specificity, positive predictive value, and negative predicative value were determined by one-way unbalanced ANOVA with an α level of 0.05. Tukey HSD post-hoc tests were used to ascertain significant differences between the passive cavitation and plane wave B-mode imaging groups.

The azimuthal positions of the maximum grayscale value and maximum acoustic power were determined for each cumulative plane wave B-mode and passive cavitation image, respectively. The azimuthal positions were determined at a fixed range position of 30 mm, the preset distance between the histotripsy focus and the imaging array (Fig. 1A). The azimuthal positions of the maximum grayscale value and maximum acoustic power were correlated with the peak negative pressure and pulse duration of the histotripsy pulse using Pearson's linear correlation coefficient. Differences in the correlation coefficients were compared using the Fisher transformation.

III. RESULTS

A. Phantom Liquefaction

Representative liquefaction zones generated in the phantom by histotripsy are shown in figures 2 and 3A. The geometry of the liquefaction zone resembled a tadpole lesion for pulses longer than 5 μs [29], with a large head and a tail that narrows distally. The liquefaction zone was elongated along the imaging azimuth (central axis of the histotripsy transducer, left to right in figures 2 and 3) compared to the imaging range dimension (up and down in figures 2 and 3). Regions of intact phantom were observed between liquefied areas for the shortest pulse duration (5 μs, Fig. 3A) at peak negative pressures 18 MPa and greater. A longer treatment time would thus be necessary for complete liquefaction within the entire focal zone for these insonation conditions.

B. Temporal Change of Bubble Cloud Grayscale Value

Strong hyperechoic interference patterns prevented analysis of the bubble clouds in the first two plane wave B-mode images, acquired 5 and 92 μs after the focal insonation. For all insonation conditions, the average grayscale value remained within 1% between 179 μs to 1 ms. The bubble cloud persisted over the 50 ms period between histotripsy pulses, by which time the grayscale value decreased by 30 ± 19% compared to the frame acquired 179 μs post focal insonation.

C. Correlation of Imaging with Phantom Liquefaction

Representative co-registered plane wave B-mode or passive cavitation images with the processed phantom images are shown in Fig. 3B and Fig. 3C, respectively. Note the strong acoustic emissions in range locations above and below the liquefaction zone, which is consistent with the poor range resolution of (1) [33], [53]. Echogenicity outside the liquefied region is also observed for plane wave B-mode imaging, though to a lesser degree compared to PCI (Fig. 3B). The
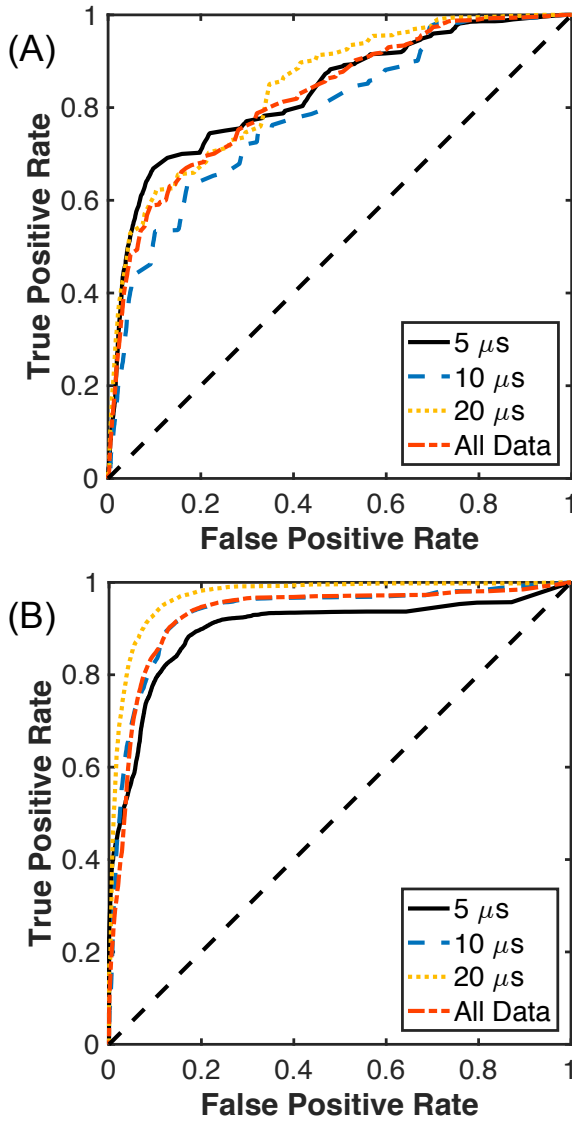
Fig. 4: Receiver operating characteristic for (A) plane wave B-mode images and (B) passive cavitation images grouped by the histotripsy pulse duration, and for all pulse durations (All Data). No compression of the passive cavitation image acoustic power or grayscale values of the plane wave B-mode images was used in the computations of these values. N = 25 for each pulse duration.

resulting ROC curves comparing plane wave B-mode or PCI to the liquefaction zone in the phantom are shown in Fig. 4. No compression of the grayscale value or acoustic power was used to compute the ROC curves in Fig. 4. When comparing all histotripsy exposure conditions, the AUROC was 0.82 ± 0.05 for the non-compressed grayscale values, and 0.78 ± 0.01 for the logarithmically compressed grayscale values. For PCI, the AUROC was 0.94 for both non-compressed and logarithmically compressed acoustic powers. In all cases, the AUROC was significantly greater than 0.5 ($p < 0.05$). The AUROCs correlating PCI with phantom liquefaction were significantly greater than plane wave B-mode imaging for each compression type ($p < 0.05$). The optimal operating point of the ROC, used to determine the pixel threshold for phantom liquefaction, was $1.94 \times 10^8 \pm 1.66 \times 10^3$ (82.90 ± 0.0004 dB re 1) for plane wave B-mode imaging and $9.36 \times 10^{10} \pm 6.42 \times 10^8$ mV^2/µs (109.73 ± 0.002 dB re 1 mV^2/µs) for PCI.

The accuracy, sensitivity, specificity, positive predictive value, and negative predicative value for PCI and plane wave B-mode imaging at their respective non-compressed threshold values are listed in Tables I and II. Except for specificity, PCI was either equivalent or improved compared to plane wave B-mode imaging. In particular, the sensitivity for PCI was 160% greater than for plane wave B-mode imaging.

D. Cavitation Monitoring

The azimuthal position relative to the free field focus of the histotripsy transducer for the maximum grayscale value and maximum acoustic power are shown in Fig. 5A and 5B, respectively. The Pearson correlation coefficients of these azimuthal locations with the histotripsy insonation parameters are listed in Table III. No correlations were observed between the azimuthal position of the maximum grayscale value and the histotripsy insonation parameters. The maximum acoustic power translated into the nearfield relative to the free field focus with increasing peak negative pressure or pulse duration. However, the maximum acoustic power typically did not extend beyond -3.5 mm for peak negative pressures greater than 18 MPa for the 20 µs pulse duration, and for peak negative pressures greater than 20 MPa for the 10 µs pulse duration. The azimuthal position of the liquefaction zone head (i.e. portion of the liquefaction zone closest to the transducer) is shown in Fig. 5C. The liquefaction zone head was closer to the histotripsy source than the maximum acoustic power or grayscale value for specific insonation conditions, as would be expected from Fig. 2. Furthermore, the liquefaction zone head moved closer to the histotripsy source with increasing peak negative pressure for pulse durations 5 and 10 µs, or increasing pulse duration for peak negative pressures 12, 18, and 20 MPa, as summarized in Table III. A stronger correlation was found between the positions of the maximum acoustic power and the liquefaction zone head ($\rho = 0.85$) than the maximum grayscale value and the liquefaction zone head ($\rho = 0.44$, Fig. 5D).

IV. Discussion

A. Correlation of Imaging with Phantom Liquefaction

In this study, the acoustic power of cavitation emissions mapped using passive cavitation imaging (PCI) was found to have a stronger correlate with phantom histotripsy liquefaction than the grayscale values of plane wave B-mode imaging. Previous studies have demonstrated that PCI can predict thermal ablation with focused ultrasound [28]-[30]. Both plane wave B-mode imaging and PCI have been used to monitor histotripsy cavitation [7], [19], but have not correlated the images with the liquefaction zone. The results presented here suggest PCI may be well suited for monitoring liquefaction with histotripsy, a therapeutic approach that exclusively utilizes cavitation.

Passive cavitation imaging generally had a better AUROC, accuracy, sensitivity, and negative predicative value than plane wave B-mode imaging (Tables I and II). Both modalities had specificity greater than 0.9. The sensitivity of PCI to phantom liquefaction was significantly improved compared to plane wave B-mode imaging, potentially due to the direct

Table I
Comparison of statistics extracted from receiver operator characteristics for passive cavitation imaging (PCI) and plane wave B-Mode imaging grouped by pulse duration (all peak negative pressures), including the area under the receiver operator characteristic (AUROC), accuracy, sensitivity, specificity, positive predictive value (PPV), and negative predicative value (NPV). No compression of the passive cavitation image acoustic power or the plane wave B-mode grayscale value was used in the computation of these values. **Bold values** indicate a significant difference between plane wave B-mode and PCI.

Pulse Duration	5 µs		10 µs		20 µs		All Pulse Durations	
Statistic	B-Mode	PCI	B-Mode	PCI	B-Mode	PCI	B-Mode	PCI
AUROC	0.83 ± 0.07	**0.89 ± 0.06**	0.78 ± 0.09	**0.95 ± 0.06**	0.84 ± 0.04	**0.97 ± 0.04**	0.82 ± 0.05	**0.94 ± 0.05**
Accuracy	0.86 ± 0.03	0.88 ± 0.03	0.83 ± 0.02	**0.90 ± 0.06**	0.81 ± 0.02	**0.92 ± 0.05**	0.83 ± 0.01	**0.90 ± 0.03**
Sensitivity	0.53 ± 0.20	**0.79 ± 0.15**	0.44 ± 0.11	**0.79 ± 0.16**	0.49 ± 0.05	**0.84 ± 0.02**	0.49 ± 0.06	**0.81 ± 0.05**
Specificity	**0.94 ± 0.03**	0.90 ± 0.07	0.95 ± 0.04	0.93 ± 0.06	0.96 ± 0.05	0.96 ± 0.05	**0.95 ± 0.01**	0.93 ± 0.02
PPV	**0.74 ± 0.06**	0.68 ± 0.01	0.72 ± 0.01	**0.78 ± 0.06**	0.85 ± 0.10	**0.90 ± 0.05**	0.78 ± 0.02	0.80 ± 0.06
NPV	0.88 ± 0.01	**0.94 ± 0.03**	0.85 ± 0.02	**0.94 ± 0.05**	0.80 ± 0.01	**0.93 ± 0.03**	0.84 ± 0.02	**0.93 ± 0.01**

Table II
Comparison of statistics extracted from receiver operator characteristics for passive cavitation imaging (PCI) and plane wave B-Mode imaging grouped by peak negative pressure (all pulse durations), including the area under the receiver operator characteristic (AUROC), accuracy, sensitivity, specificity, positive predictive value (PPV), and negative predicative value (NPV). No compression of the passive cavitation image acoustic power or the plane wave B-mode grayscale value was used in the computation of these values. **Bold values** indicate a significant difference between plane wave B-mode and PCI.

Peak Negative Pressure	12 MPa		15 MPa		18 MPa		20 MPa		23 MPa	
Statistic	B-Mode	PCI	B-Mode	PCI	B-Mode	PCI	B-Mode	PCI	B-Mode	PCI
AUROC	0.68 ± 0.05	**0.85 ± 0.09**	0.88 ± 0.07	**0.96 ± 0.05**	0.84 ± 0.10	**0.97 ± 0.04**	0.88 ± 0.07	0.95 ± 0.06	0.81 ± 0.06	**0.96 ± 0.03**
Accuracy	0.84 ± 0.06	0.88 ± 0.07	0.88 ± 0.07	0.91 ± 0.07	0.83 ± 0.05	**0.92 ± 0.07**	0.82 ± 0.05	**0.89 ± 0.05**	0.78 ± 0.04	**0.90 ± 0.05**
Sensitivity	0.30 ± 0.13	**0.50 ± 0.22**	0.51 ± 0.18	0.65 ± 0.20	0.56 ± 0.23	**0.78 ± 0.13**	0.53 ± 0.19	**0.82 ± 0.13**	0.49 ± 0.09	**0.88 ± 0.11**
Specificity	0.96 ± 0.04	0.96 ± 0.05	0.98 ± 0.04	0.97 ± 0.05	0.93 ± 0.06	0.97 ± 0.03	0.94 ± 0.06	0.92 ± 0.08	0.94 ± 0.08	0.90 ± 0.07
PPV	0.60 ± 0.16	0.71 ± 0.14	0.85 ± 0.20	0.87 ± 0.08	0.77 ± 0.08	**0.92 ± 0.05**	0.78 ± 0.01	0.80 ± 0.06	0.81 ± 0.04	0.83 ± 0.03
NPV	0.86 ± 0.04	0.90 ± 0.04	0.89 ± 0.04	0.92 ± 0.06	0.84 ± 0.04	**0.92 ± 0.07**	0.83 ± 0.06	**0.93 ± 0.03**	0.78 ± 0.05	**0.94 ± 0.05**

mapping of the received cavitation emission power with PCI. Plane wave B-mode imaging denotes the presence of a hyperechoic bubble cloud, but does not indicate which portions of the bubble clouds are undergoing strong mechanical action. Additionally, persistent bubble clouds occur when the pulse repetition frequency of the histotripsy pulse exceeds 1 Hz [59], consistent with the observation in this study with high frame rate plane wave imaging. The persistent bubble cloud attenuates liquefaction [9], [59], but remains hyperechoic. Other clinical contrast-enhanced ultrasound pulsing schemes, such as pulse inversion, also only indicate the presence of cavitation and not the cavitation emission power. Feedback with PCI could account for persistent bubble clouds by detecting shadowed regions in the focal zone containing bubbles but undergoing limited mechanical activity [60].

The increased sensitivity of PCI to phantom liquefaction compared to plane wave imaging suggests it may also be useful in pretreatment planning of histotripsy liquefaction. The beam profile of scattered ultrasound pulses in the absence of cavitation have been successful mapped utilizing PCI [53]. A similar technique could be utilized for low amplitude, non-ablative histotripsy pulses to enable steering of the focus through aberrative media to the intended target.

Passive cavitation images were analyzed in terms of the radiated acoustic power in this study [7], although the energy of the acoustic emissions could also be compared to phantom liquefaction [49], [61]. No difference in the AUROCs was observed between passive cavitation images analyzed in terms of the power or energy of the acoustic emissions (0.94 for both). Thus, the power and the energy of acoustic emissions from the bubble cloud provide equally useful correlations with phantom liquefaction.

In this study, PCI and plane wave B-mode imaging were correlated with phantom liquefaction. Magnetic resonance (MR) imaging is also utilized clinically for assessing changes in soft tissue properties [62]. Although MR imaging has only been employed clinically to assess lesions from thermal HIFU [63], it has shown promise for assessing histotripsy lesions at high magnetic field strengths (4.7-9 T) [14], [15], [64]. Visualization of the lesion will occur only after significant changes in the tissue structure, and would not provide information about mechanical action induced by the histotripsy pulse. PCI quantifies the spatial location and power of acoustic emissions from the bubble cloud, a surrogate for its mechanical action [65]. A disadvantage of PCI is its inability to provide direct visualization of tissue liquefaction. A possible route for image guidance would be to combine PCI
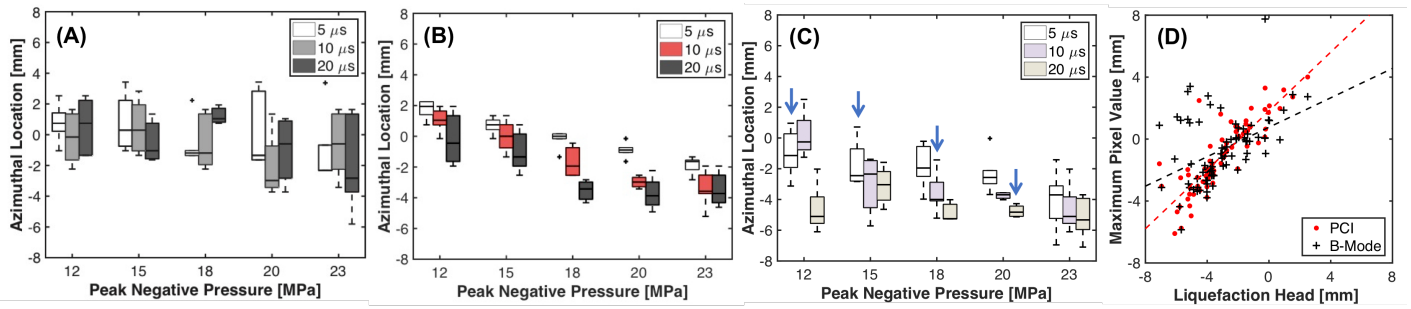
Fig. 5: Boxplot of the azimuthal position relative to the free field focus of the histotripsy transducer of (a) the maximum grayscale value, (b) maximum acoustic power, and (c) the liquefaction zone head. The pulse duration of the histotripsy insonation is indicated in the legend. The solid black line indicates the median value, the box extends from the 25th to the 75th quartiles, and the dashed whiskers span the range of the data. Arrows in (c) indicate the position of the liquefaction zone head is significantly different than the position of the maximum grayscale value or acoustic power. (d) Scatter plot of the azimuthal position of the front face of the liquefaction zone head and the maximum acoustic power or maximum grayscale value. The dashed lines are linear regression curves between the maximum acoustic power or grayscale value and position of the liquefaction zone head. N = 5 for each set of insonation conditions.

for real-time feedback of the nature and location of the bubble cloud's mechanical action, and MR imaging for assessment of tissue liquefaction.

B. Monitoring Cavitation Dynamics

Strong acoustic emissions and hyperechoic bubble clouds were observed for all insonation conditions. Interestingly, two local maxima in the grayscale value and emission power were often observed along the azimuth (Fig. 3), indicating multiple locations of intense cavitation activity. Analysis of high speed videography has shown that the bubble cloud forms through scattering of the incident shocked pulse from expanded nuclei in the focal zone [16]. The structure of the detected cavitation signals may reflect this process, with peaks proximal to the histotripsy source indicating regions of shock wave scattering and distal peak corresponding to the expanded nuclei in the focal zone. Further studies are required to correlate the structure of the passive cavitation or plane wave B-mode image with the bubble cloud dynamics assessed with high speed videography.

The location of the most intense portions of mechanical activity were dependent on the histotripsy insonation parameters, as indicated in Fig. 5B. The location of the liquefaction zone head was also dependent on the insonation conditions, but only for select histotripsy insonation parameters (Table III). In contrast, the location of the most

Table III
Pearson correlation coefficients between the azimuthal position of the maximum pixel or the liquefaction zone head (LZH), and the histotripsy insonation parameters. Gray shaded cells indicate correlation of the parameter with the peak negative pressure at fixed pulse duration. Green shaded cells indicate correlation of the parameter with the pulse duration at a fixed peak negative pressure. An asterisk denotes statistical significance ($p < 0.05$).

	Azimuthal Position		
	B-Mode	PCI	LZH
Pulse Duration [µs]			
5	-0.33	-0.93*	-0.54*
10	0.22	-0.89*	-0.68*
20	0.27	-0.74*	-0.32
Peak Negative Pressure [MPa]			
12	-0.00	-0.65*	-0.74*
15	-0.40	-0.59*	-0.29
18	0.46	-0.87*	-0.68*
20	-0.16	-0.82*	-0.77*
23	-0.19	-0.48*	-0.30

hyperechoic portions of the bubble cloud were independent of the histotripsy parameters.

The correlations observed with PCI highlight its usefulness for monitoring cavitation dynamics [61]. Passive cavitation imaging provides information not only about the amplitude of acoustic emission, but their spatial location as well. By direct mapping of the emissions, this approach overcomes the tradeoff between sensitivity and specificity associated with single element passive cavitation detectors [49]. By tracking cavitation emissions over an extended area, observations in this study denoted translation of the maximum acoustic power closer to the histotripsy source with increasing pulse duration (Fig. 5B). The proximal face of the bubble cloud is the most significant source of acoustic emissions [16], thus it would be expected that the azimuthal location of the maximum acoustic power would move towards the transducer face. For the 20 µs pulse duration, the azimuthal location of the maximum acoustic power translated for peak negative pressures 12 – 15 MPa, but remained spatially fixed for peak negative pressures greater than 18 MPa. The saturation of the azimuthal position may indicate that the bubble cloud has grown to the edge of the focal zone, which has been demonstrated to halt the cloud growth [66].

No changes were observed in the azimuthal location of the maximum grayscale value with the histotripsy insonation parameters. The most hyperechoic portions of the bubble cloud may preferentially occur at a fixed location due to the shock-scattering nature of the bubble cloud formation. Alternatively, the fixed delay between the plane wave B-mode image acquisition and histotripsy pulse initiation may bias the location of the cloud. Further study with high frame rate plane wave imaging may help to elucidate the temporal evolution of the hyperechogenicity of the bubble cloud [18], [19]. The spatial shift in the strongest acoustic emissions with the insonation parameters is also reflected in the position of the liquefaction zone, which further emphasizes the need to use detection methods such as PCI to monitor cavitation information over an extended area.

C. Study Limitations

Images were analyzed at a fixed range depth of 30 mm. The range resolution of PCI is limited compared to B-mode imaging due to an elongation of the point spread function of the linear imaging array [27]. Bubble clouds generated by

histotripsy pulses grow predominately along the central axis of the histotripsy transducer [16]. An imaging window along the central axis of the histotripsy transducer would be sufficient to monitor ablative cavitation activity. For alternative orientations of the imaging array, modifications of (1) may be necessary to achieve adequate imaging range resolution. The adaptive robust Capon beamformer [33] increases the range resolution, albeit at an increased computational load. Frequency-sum PCI has also been shown to improve image resolution, though this algorithm is more susceptible to image artifacts from noise [67].

The free field focus of the histotripsy transducer was located with hyperechoic bubble clouds generated from 5 µs histotripsy pulses [5], [10]. The bubble cloud grows azimuthally into the nearfield compared to the geometric focus of the histotripsy transducer [68]. For a 5 µs histotripsy pulse, the bubble cloud would be approximately 1 mm in diameter [16]. Thus, the reported azimuthal positions reported in Fig. 5 are shifted by 1 mm relative to the geometric focus of the histotripsy transducer.

A tissue prostate phantom was used in this study instead of viable tissue. The use of a phantom allowed specified, consistent medium properties [39]. Fiducial markers embedded within the phantom allowed for precise registration of the PCI and plane wave B-mode imaging with the histological images. However, this *in vitro* approach may not be representative of tissue liquefaction *in vivo*. The population of cavitation nuclei may not replicate that found in real tissue, altering the threshold for individual bubble formation. However, the bubble dynamics initiated by highly shocked histotripsy excitations are largely independent of the initial bubble diameter and the viscoelastic properties of the medium [46], [68]. A lack of scatterers used in the phantom minimized the presence of cavitation nuclei, but also resulted in a medium that was more hypoechoic than tissue [50]. Ultrasound images (PCI and plane wave B-mode imaging) were also only acquired in a fixed two-dimensional plane, whereas a volume of the phantom was ablated.

The image acquisition time relative to the histotripsy focal insonation differed between the passive cavitation images and plane wave B-mode images (Fig. 1B). As a passive technique, PCI requires that the image acquisition occur during insonation. Similar to prior studies, plane wave B-mode imaging was performed after the histotripsy insonation to avoid hyperechoic interference lines that substantially reduce the image quality [19]-[21]. Observations with high speed videography indicate that the bubble cloud grows slightly after the completion of the histotripsy insonation, but collapses within 50–200 µs depending on the size of the cloud [16]. Residual bubbles have been observed up to 30 ms after the collapse [17], [18]. Plane-wave B-mode images in this study were acquired 1 ms after insonation, though little change was observed in the grayscale value of the bubble cloud between 179 µs and 1 ms. Thus, the hyperechoic bubble clouds observed in this study with plane wave B-mode imaging may be due to residual bubbles and not the original bubble cloud responsible for inducing mechanical liquefaction. The correlation between phantom liquefaction and plane wave B-mode images may be better for images acquired at alternate

times, or using alternate B-mode image acquisition methods (e.g. plane wave versus conventional [13]).

It should also be noted that the optimal operating points extracted from the ROC curves will vary based on the array sensitivity and the depth of the histotripsy excitation. System independent PCI requires accounting for the element sensitivities [69]. Existing approaches to quantitate scattering also do not account for dense bubble clouds, such as those generated during histotripsy [33]. Furthermore, the optimal operating points may vary between the phantom and living tissue due to difference in structural composition, and may be tissue specific. Nevertheless, the results of this study indicate PCI provides an improved correlation with phantom liquefaction from histotripsy, albeit with a limited range resolution.

In this study, phantom liquefaction occurred over the course of approximately 100 s (2000 pulses delivered at 20 Hz). Although the number of pulses delivered may be excessive for complete liquefaction of the focal zone for most insonation conditions [3], only partial liquefaction of the focal zone was noted for the 5 µs pulse duration (Fig. 3). Future developments of PCI to monitor histotripsy-mediated tissue liquefaction will be needed to determine suitable treatment endpoints and minimize treatment time. Passive cavitation imaging could be utilized to monitor the cumulative cavitation emissions, which in turn can be used as a decision-making tool for determining when to stop the treatment. By delivering only the necessary number of histotripsy pulses for liquefaction, the treatment time may be reduced and off target or other undesired effects minimized.

IV. CONCLUSIONS

Passive cavitation and plane wave B-mode imaging were utilized to observe cavitation and correlated with liquefaction locations within a prostate tissue phantom exposed to histotripsy pulses. Passive cavitation images had significantly larger areas under the receiver operator characteristic, sensitivity, and accuracy when correlated with phantom liquefaction compared to plane wave B-mode imaging, but similar specificity. Correlations were observed between all histotripsy insonation parameters and the azimuthal location of the PCI maximum acoustic power along the axis of the histotripsy transducer.

REFERENCES

[1]   F. A. Jolesz, "MRI-Guided Focused Ultrasound Surgery," *Annu. Rev. Med.*, vol. 60, no. 1, pp. 417–430, Feb. 2009.

[2]   J. Tavakkoli and N. T. Sanghvi, "Ultrasound-guided HIFU and thermal ablation," in *Therapeutic Ultrasound: Mechanisms to applications*, 1st ed., V. Frenkel, Ed., New York: Nova Science Publishers, 2011, pp. 137-161.

[3]   A. Maxwell, O. Sapozhnikov, M. Bailey, L. Crum, Z. Xu, B. Fowlkes, C. Cain, and V. Khokhlova, "Disintegration of tissue using high intensity focused ultrasound: two approaches that utilize shock waves," *Acoust. Today*, vol. 8, no. 4, pp. 24–37, 2012.

[4]   V. A. Khokhlova, J. B. Fowlkes, W. W. Roberts, G. R. Schade, Z. Xu, T. D. Khokhlova, T. L. Hall, A. D. Maxwell, Y.-N. Wang, and C. A. Cain, "Histotripsy methods in mechanical disintegration of tissue: Towards clinical applications," *Int J Hyperthermia*, vol. 31, no. 2, pp. 145–162, Mar. 2015.

[5] A. D. Maxwell, G. Owens, H. S. Gurm, K. Ives, D. D. Myers Jr, and Z. Xu, "Noninvasive Treatment of Deep Venous Thrombosis Using Pulsed Ultrasound Cavitation Therapy (Histotripsy) in a Porcine Model," *J. Vasc. Intervent. Radiol.*, vol. 22, no. 3, pp. 369–377, Mar. 2011.

[6] X. Zhang, G. E. Owens, H. S. Gurm, Y. Ding, C. A. Cain, and Z. Xu, "Noninvasive thrombolysis using histotripsy beyond the intrinsic threshold (microtripsy)," *IEEE Trans. Ultrason., Ferroelect., Freq. Contr.*, vol. 62, no. 7, pp. 1342–1355, Jul. 2015.

[7] K. B. Bader, K. J. Haworth, H. Shekhar, A. D. Maxwell, T. Peng, D. D. McPherson, and C. K. Holland, "Efficacy of histotripsy combined with rt-PA in vitro," *Phys. Med. Biol.*, vol. 61, no. 14, pp. 5253–5274, Jun. 2016.

[8] Z. Xu, G. Owens, D. Gordon, C. Cain, and A. Ludomirsky, "Noninvasive Creation of an Atrial Septal Defect by Histotripsy in a Canine Model," *Circulation*, vol. 121, no. 6, pp. 742–749, Feb. 2010.

[9] A. P. Duryea, W. W. Roberts, C. A. Cain, and T. L. Hall, "Removal of residual cavitation nuclei to enhance histotripsy erosion of model urinary stones," *IEEE Trans. Ultrason., Ferroelect., Freq. Contr.*, vol. 62, no. 5, pp. 896–904, 2015.

[10] E. Vlaisavljevich, Y. Kim, S. Allen, G. Owens, S. Pelletier, C. Cain, K. Ives, and Z. Xu, "Image-guided non-invasive ultrasound liver ablation using histotripsy," *Ultrasound Med. Biol.*, vol. 39, no. 8, pp. 1398–1409, Aug. 2013.

[11] T. L. Hall, C. R. Hempel, A. M. Lake, K. Kieran, K. Ives, J. B. Fowlkes, C. A. Cain, and W. W. Roberts, "Histotripsy for the treatment of BPH: evaluation in a chronic canine model," presented at the IEEE Ultrasonics Symposium, 2008, pp. 765–767.

[12] "Safety and Initial Efficacy Study of the Vortx Rx for Treatment of Benign Prostatic Hyperplasia (US) ," *clinicaltrials.gov*. [Online]. Available: http://clinicaltrials.gov/ct2/show/NCT01896973?term=Vortx+Rx &rank=1. [Accessed: 24-Mar-2014].

[13] T. Hall, J. Fowlkes, and C. Cain, "A real-time measure of cavitation induced tissue disruption by ultrasound imaging backscatter reduction," *IEEE Trans. Ultrason., Ferroelect., Freq. Contr.*, vol. 54, no. 3, pp. 569–575, Mar. 2007.

[14] S. P. Allen, T. L. Hall, C. A. Cain, and L. Hernandez-Garcia, "Controlling cavitation-based image contrast in focused ultrasound histotripsy surgery," *Magn. Reson. Med.*, vol. 73, no. 1, pp. 204–213, Jan. 2014.

[15] S. P. Allen, L. Hernandez-Garcia, C. A. Cain, and T. L. Hall, "MR-based detection of individual histotripsy bubble clouds formed in tissues and phantoms," *Magn. Reson. Med.*, vol. 76, no. 5, pp. 1486–1493, Nov. 2015.

[16] A. D. Maxwell, T.-Y. Wang, C. A. Cain, J. B. Fowlkes, O. A. Sapozhnikov, M. R. Bailey, and Z. Xu, "Cavitation clouds created by shock scattering from bubbles during histotripsy," *J. Acoust. Soc. Am.*, vol. 130, no. 4, p. 1888, 2011.

[17] Z. Xu, T. L. Hall, J. B. Fowlkes, and C. A. Cain, "Optical and acoustic monitoring of bubble cloud dynamics at a tissue-fluid interface in ultrasound tissue erosion," *J. Acoust. Soc. Am.*, vol. 121, no. 4, pp. 2421–10, 2007.

[18] F. Prieur, A. Zorgani, S. Catheline, R. Souchon, J.-L. Mestas, M. Lafond, and C. Lafon, "Observation of a cavitation cloud in tissue using correlation between ultrafast ultrasound images," *IEEE Trans. Ultrason., Ferroelect., Freq. Contr.*, vol. 62, no. 7, pp. 1256–1264, Jul. 2015.

[19] J. Gateau, J.-F. Aubry, M. Pernot, M. Fink, and M. Tanter, "Combined passive detection and ultrafast active imaging of cavitation events induced by short pulses of high-intensity ultrasound," *IEEE Trans. Ultrason., Ferroelect., Freq. Contr.*, vol. 58, no. 3, pp. 517–532, Mar. 2011.

[20] H. Hu, S. Xu, Y. Yuan, R. Liu, S. Wang, and M. Wan, "Spatial-temporal ultrasound imaging of residual cavitation bubbles around a fluid–tissue interface in histotripsy," *J. Acoust. Soc. Am.*, vol. 137, no. 5, pp. 2563–2572, May 2015.

[21] B. Arnal, J. Baranger, C. Demene, M. Tanter, and M. Pernot, "In vivo real-time cavitation imaging in moving organs," *Phys. Med. Biol.*, vol. 62, no. 3, pp. 843–857, Jan. 2017.

[22] X. Zhang, R. M. Miller, K.-W. Lin, A. M. Levin, G. E. Owens, H. S. Gurm, C. A. Cain, and Z. Xu, "Real-time feedback of histotripsy thrombolysis using bubble-induced color Doppler," *Ultrasound Med. Biol.*, vol. 41, no. 5, pp. 1386–1401, May 2015.

[23] T.-Y. Wang, T. Hall, Z. Xu, J. B. Fowlkes, C. A. Cain, and T. L. Hall, "Imaging feedback of histotripsy treatments using ultrasound shear wave elastography," *IEEE Trans. Ultrason., Ferroelect., Freq. Contr.*, vol. 59, no. 6, pp. 1167–1181, Jun. 2012.

[24] R. M. Miller, X. Zhang, A. D. Maxwell, C. A. Cain, and Z. Xu, "Bubble-Induced Color Doppler Feedback for Histotripsy Tissue Fractionation," *IEEE Trans. Ultrason., Ferroelect., Freq. Contr.*, vol. 63, no. 3, pp. 408–419, Mar. 2016.

[25] E. Vlaisavljevich, J. Greve, X. Cheng, K. Ives, J. Shi, L. Jin, A. Arvidson, T. Hall, T. H. Welling, G. Owens, W. Roberts, and Z. Xu, "Non-Invasive Ultrasound Liver Ablation Using Histotripsy: Chronic Study in an In Vivo Rodent Model," *Ultrasound Med. Biol.*, vol. 42, no. 8, pp. 1890–1902, Aug. 2016.

[26] M. Gyöngy, M. Arora, J. A. Noble, and C. C. Coussios, "Use of passive arrays for characterization and mapping of cavitation activity during HIFU exposure," presented at the IEEE Ultrasonics Symposium (IUS), 2008, pp. 871–874.

[27] V. A. Salgaonkar, S. Datta, C. K. Holland, and T. D. Mast, "Passive cavitation imaging with ultrasound arrays," *J. Acoust. Soc. Am.*, vol. 126, no. 6, p. 3071, 2009.

[28] C. R. Jensen, R. W. Ritchie, M. Gyöngy, J. R. Collin, T. Leslie, and C.-C. Coussios, "Spatiotemporal monitoring of high-intensity focused ultrasound therapy with passive acoustic mapping," *Radiol.*, vol. 262, no. 1, pp. 252–261, 2012.

[29] K. J. Haworth, V. A. Salgaonkar, N. M. Corregan, C. K. Holland, and T. D. Mast, "Using passive cavitation images to classify high-intensity focused ultrasound lesions," *Ultrasound Med. Biol.*, vol. 41, no. 9, pp. 2420–2434, Sep. 2015.

[30] C. D. Arvanitis and N. McDannold, "Integrated ultrasound and magnetic resonance imaging for simultaneous temperature and cavitation monitoring during focused ultrasound therapies," *Med. Phys.*, vol. 40, no. 11, pp. 112901–15, Nov. 2013.

[31] J. J. Choi, R. C. Carlisle, C. Coviello, L. Seymour, and C.-C. Coussios, "Non-invasive and real-time passive acoustic mapping of ultrasound-mediated drug delivery," *Phys. Med. Biol.*, vol. 59, no. 17, pp. 4861–4877, Aug. 2014.

[32] K. J. Haworth, J. L. Raymond, K. Radhakrishnan, M. R. Moody, S.-L. Huang, T. Peng, H. Shekhar, M. E. Klegerman, H. Kim, D. D. McPherson, and C. K. Holland, "Trans-Stent B-Mode Ultrasound and Passive Cavitation Imaging," *Ultrasound Med. Biol.*, vol. 42, no. 2, pp. 518–527, Feb. 2016.

[33] C. Coviello, R. Kozick, J. Choi, M. Gyöngy, C. Jensen, P. P. Smith, and C.-C. Coussios, "Passive acoustic mapping utilizing optimal beamforming in ultrasound therapy monitoring," *J. Acoust. Soc. Am.*, vol. 137, no. 5, pp. 2573–2585, May 2015.

[34] J. J. Kwan, R. Myers, C. M. Coviello, S. M. Graham, A. R. Shah, E. Stride, R. C. Carlisle, and C.-C. Coussios, "Ultrasound-Propelled Nanocups for Drug Delivery," *Small*, vol. 11, no. 39, pp. 5305–5314, Aug. 2015.

[35] A. D. Maxwell, T. Y. Wang, L. Yuan, A. P. Duryea, and Z. Xu, "A tissue phantom for visualization and measurement of ultrasound-induced cavitation damage," *Ultrasound Med. Biol.*, vol. 36, no. 12, pp. 2132–2143, 2010.

[36] E. Vlaisavljevich, Y. Kim, G. Owens, W. Roberts, C. Cain, and Z. Xu, "Effects of tissue mechanical properties on susceptibility to histotripsy-induced tissue damage," *Phys. Med. Biol.*, vol. 59, no. 2, pp. 253–270, Dec. 2013.

[37] E. Vlaisavljevich, K.-W. Lin, M. T. Warnez, R. Singh, L. Mancia, A. J. Putnam, E. Johnsen, C. Cain, and Z. Xu, "Effects of tissue stiffness, ultrasound frequency, and pressure on histotripsy-induced cavitation bubble behavior," *Phys. Med. Biol.*, pp. 2271–2292, Feb. 2015.

[38] K. W. Lin, Y. Kim, A. Maxwell, T. Y. Wang, and T. Hall, "Histotripsy beyond the intrinsic cavitation threshold using very short ultrasound pulses: microtripsy.," *IEEE Trans. Ultrason., Ferroelect., Freq. Contr.*, vol. 61, no. 2, pp. 251–265, 2014.

[39] K. B. Bader, M. J. Crowe, J. L. Raymond, and C. K. Holland, "Effect of Frequency-Dependent Attenuation on Predicted Histotripsy Waveforms in Tissue-Mimicking Phantoms," *Ultrasound Med. Biol.*, vol. 42, no. 7, pp. 1701–1705, Jul. 2016.

[40] J. Xu, T. A. Bigelow, G. Davis, A. Avendano, P. Shrotriya, K. Bergler, and Z. Hu, "Dependence of ablative ability of high-intensity focused ultrasound cavitation-based histotripsy on mechanical properties of agar," *J. Acoust. Soc. Am.*, vol. 136, no. 6, pp. 3018–3027, Dec. 2014.

[41] V. Normand, D. L. Lootens, E. Amici, K. P. Plucknett, and P. Aymard, "New Insight into Agarose Gel Mechanical Properties," *Biomacromolecules*, vol. 1, no. 4, pp. 730–738, Dec. 2000.

[42] L. Zhai, J. Madden, W. C. Foo, and V. Mouraviev, "Characterizing stiffness of human prostates using acoustic radiation force," *Ultrasonic Imag.*, vol. 32, no. 4, pp. 201–213, 2010.

[43] S. Fu, M. Zhang, Y. Wang, Q. Li, and J. Tang, "Prostatic Elasticity: A New Non-invasive Parameter to Assess Bladder Outlet Obstruction Caused by Benign Prostatic Hyperplasia (a Canine Experiment)," *Urology*, vol. 82, no. 5, pp. 1114–1119, 2013.

[44] M. Zhang, S. Fu, Y. Zhang, J. Tang, and Y. Zhou, "Elastic Modulus of the Prostate: A New Non-invasive Feature to Diagnose Bladder Outlet Obstruction in Patients with Benign Prostatic Hyperplasia," *Ultrasound Med. Biol.*, vol. 40, no. 7, pp. 1408–1413, Jul. 2014.

[45] T. Hall and C. Cain, "A low cost compact 512 channel therapeutic ultrasound system for transcutaneous ultrasound surgery," *AIP Conf. Proc.,* vol. 829, p. 445, 2006.

[46] A. D. Maxwell, C. A. Cain, T. L. Hall, J. B. Fowlkes, and Z. Xu, "Probability of Cavitation for Single Ultrasound Pulses Applied to Tissues and Tissue-Mimicking Materials," *Ultrasound Med. Biol.*, vol. 39, no. 3, pp. 449–465, Mar. 2013.

[47] M. S. Canney, V. A. Khokhlova, O. V. Bessonova, M. R. Bailey, and L. A. Crum, "Shock-Induced Heating and Millisecond Boiling in Gels and Tissue Due to High Intensity Focused Ultrasound," *Ultrasound Med. Biol.*, vol. 36, no. 2, pp. 250–267, 2010.

[48] P. B. Rosnitskiy, P. V. Yuldashev, O. A. Sapozhnikov, A. D. Maxwell, W. Kreider, M. R. Bailey, and V. A. Khokhlova, "Design of HIFU Transducers for Generating Specified Nonlinear Ultrasound Fields," *IEEE Trans. Ultrason., Ferroelect., Freq. Contr.*, vol. 64, no. 2, pp. 374–390, Jan. 2017.

[49] K. J. Haworth, K. B. Bader, K. T. Rich, C. K. Holland, and T. D. Mast, "Quantitative Frequency-Domain Passive Cavitation Imaging," *IEEE Trans. Ultrason., Ferroelect., Freq. Contr.*, vol. 64, no. 1, pp. 177–191, Jan. 2017.

[50] T. L. Szabo, *Diagnostic Ultrasound Imaging: Inside Out (Biomedical Engineering)*, 1st ed. Academic Press, 2004.

[51] K. E. Hitchcock, N. M. Ivancevich, K. J. Haworth, D. N. C. Stamper, D. C. Vela, J. T. Sutton, G. J. Pyne-Geithman, and C. K. Holland, "Ultrasound-enhanced rt-PA Thrombolysis in an ex vivo Porcine Carotid Artery Model," *Ultrasound Med. Biol.*, vol. 37, no. 8, pp. 1240–1251, Aug. 2011.

[52] J. J. Choi and C.-C. Coussios, "Spatiotemporal evolution of cavitation dynamics exhibited by flowing microbubbles during ultrasound exposure," *J. Acoust. Soc. Am.*, vol. 132, no. 5, p. 3538, 2012.

[53] K. J. Haworth, T. D. Mast, K. Radhakrishnan, M. T. Burgess, J. A. Kopechek, S.-L. Huang, D. D. McPherson, and C. K. Holland, "Passive imaging with pulsed ultrasound insonations," *J. Acoust. Soc. Am.*, vol. 132, no. 1, p. 544, 2012.

[54] C. Arvanitis, C. Crake, N. McDannold, and G. Clement, "Passive Acoustic Mapping with the Angular Spectrum Method," *IEEE Trans. Med. Imaging*, vol. 36, no. 4, pp. 983–993, Dec. 2016.

[55] J. A. Hanley and B. J. McNeil, "The meaning and use of the area under a receiver operating characteristic (ROC) curve.," *Radiol.y*, vol. 143, pp. 29–36, 1982.

[56] M. H. Zweig and G. Campbell, "Receiver-operating characteristic (ROC) plots: a fundamental evaluation tool in clinical medicine.," *Clin. Chem.*, vol. 39, no. 4, pp. 561–577, Apr. 1993.

[57] B. Efron, "Bootstrap Methods: Another Look at the Jackknife," *Ann. Stat.*, vol. 7, no. 1, pp. 1–26, Jan. 1979.

[58] E. R. DeLong, D. M. DeLong, and D. L. Clarke-Pearson, "Comparing the areas under two or more correlated receiver operating characteristic curves: a nonparametric approach.," *Biometrics*, vol. 44, no. 3, pp. 837–845, Sep. 1988.

[59] T.-Y. Wang, Z. Xu, T. L. Hall, J. B. Fowlkes, and C. A. Cain, "An Efficient Treatment Strategy for Histotripsy by Removing Cavitation Memory," *Ultrasound Med. Biol.*, vol. 38, no. 5, pp. 753–766, May 2012.

[60] M. A. O'Reilly and K. Hynynen, "Blood-Brain Barrier: Real-time Feedback-controlled Focused Ultrasound Disruption by Using an Acoustic Emissions-based Controller," *Radiol.*, vol. 263, no. 1, pp. 96–106, Mar. 2012.

[61] M. Gyöngy and C.-C. Coussios, "Passive cavitation mapping for localization and tracking of bubble dynamics," *J. Acoust. Soc. Am.*, vol. 128, no. 4, pp. EL175–EL180, Oct. 2010.

[62] M. Sadinski, M. Medved, I. Karademir, S. Wang, Y. Peng, Y. Jiang, S. Sammet, G. Karczmar, and A. Oto, "Short-term reproducibility of apparent diffusion coefficient estimated from diffusion-weighted MRI of the prostate," *Abdom. Imag.*, vol. 40, pp. 2423–2528, Apr. 2015.

[63] K. Hynynen and N. McDannold, "MRI guided and monitored focused ultrasound thermal ablation methods: a review of progress," *Int J Hyperthermia*, vol. 20, no. 7, pp. 725–737, Jul. 2009.

[64] T. D. Khokhlova, M. S. Canney, D. Lee, K. I. Marro, L. A. Crum, V. A. Khokhlova, and M. R. Bailey, "Magnetic resonance imaging of boiling induced by high intensity focused ultrasound," *J. Acoust. Soc. Am.*, vol. 125, no. 4, pp. 2420–2431, Apr. 2009.

[65] K. B. Bader, J. Mobley, C. C. Church, and D. F. Gaitan, "The effect of static pressure on the strength of inertial cavitation events," *J. Acoust. Soc. Am.*, vol. 132, no. 4, p. 2286, 2012.

[66] T.-Y. Wang, A. D. Maxwell, S. Park, Z. Xu, J. B. Fowlkes, C. A. Cain, K. Hynynen, and J. Souquet, "Why Are Short Pulses More Efficient in Tissue Erosion Using Pulsed Cavitational Ultrasound Therapy (Histotripsy)?," *AIP. Conf. Proc.*, no. 40, pp. 1215, 2010.

[67] S. H. Abadi, M. J. Van Overloop, and D. R. Dowling, "Frequency-sum beamforming in an inhomogeneous environment," *Proc. Meet. Acoust.*, vol. 19, p. 055080, 2013.

[68] K. B. Bader and C. K. Holland, "Predicting the growth of nanoscale nuclei by histotripsy pulses," *Phys. Med. Biol.*, pp. 2947–2966, Mar. 2016.

[69] K. T. Rich and T. D. Mast, "Methods to calibrate the absolute receive sensitivity of single-element, focused transducers," *J. Acoust. Soc. Am.*, vol. 138, no. 3, pp. EL193–EL198, Sep. 2015.